Journal of Inorganic Biochemistry 192 (2019) 52–61

Contents lists available at ScienceDirect

Journal of Inorganic Biochemistry

journal homepage: www.elsevier.com/locate/jinorgbio

Half-sandwich iridium(III) complexes with α-picolinic acid frameworks and antitumor applications

Hailong Hao[a], Xicheng Liu[a,*], Xingxing Ge[a], Yao Zhao[b], Xue Tian[a], Ting Ren[a], Yan Wang[a], Chengfeng Zhao[a], Zhe Liu[a,*]

[a] Institute of Anticancer Agents Development and Theranostic Application, The Key Laboratory of Life-Organic Analysis, Key Laboratory of Pharmaceutical Intermediates and Analysis of Natural Medicine, Department of Chemistry and Chemical Engineering, Qufu Normal University, Qufu 273165, China
[b] CAS Key Laboratory of Analytical Chemistry for Living Biosystems, Institute of Chemistry, Chinese Academy of Sciences, Beijing 100190, PR China

ARTICLE INFO

Keywords:
Half-sandwich structure
Iridium complexes
α-Picolinic acid
Antitumor

ABSTRACT

Eight half-sandwich iridium^{III} (Ir^{III}) complexes of the general formula [(η^5-Cp^{xbiph})Ir(OˆN)Cl] (Cp^{xbiph} is tetramethyl(biphenyl)cyclopentadienyl, and the OˆN is α-picolinic acid chelating ligand and its derivatives) were synthesized and characterized. Compared with *cis*-platin widely used in clinic, target Ir^{III} complexes showed at most five times more potent antitumor activity against A549 cells by the MTT (3-(4,5-dimethylthiazol-2-yl)-2,5-diphenyltetrazolium bromide) assay. Ir^{III} complexes could be transported by serum albumin, bind with DNA, catalyze the oxidation of nicotinamide-adenine dinucleotid (NADH) and induce the production of reactive oxygen species, which confirmed the antitumor mechanism of oxidation. Ir^{III} complexes could enter A549 cells followed by an energy-dependent cellular uptake mechanism, meanwhile, target the mitochondria and lysosomes with the Pearson's colocalization coefficient of 0.33 and 0.74, respectively, lead to the lysosomal destruction and the change of mitochondrial membrane potential ($\Delta\Psi m$), and eventually induce apoptosis.

1. Introduction

Platinum-based antitumor drugs have proved to be indispensable in the treatment of cancer, and accounting for almost 50% cancer therapeutic drugs on a world scale [1,2]. However, widely used it is today, platinum antitumor drugs [3] also show some adverse factors, such as unclear mechanism of action, poor selectivity, strong resistance and serious side effects, which prompted to seek the alternative antitumor drugs with more efficient and better targeted [4,5]. Ir^{III} complexes have recently emerged as the potential alternatives, compared with the conventional platinum-based drugs, which have shown favorable antiproliferative activity and a diverse antitumor mechanism [1,6].

Ir^{III} antitumor complexes included two main types: half-sandwich iridium complexes and cyclometalated iridium. Because of the excellent antitumor activity, half-sandwich structure Ir^{III} complexes have attracted much attention [7]. The general formula of half-sandwich Ir^{III} complexes is [(Cp*)Ir(LˆL)Z]PF_6, where Cp* represents the electron-rich cyclopentadienyl group or its derivatives, and Z is the leaving group, LˆL is various chelating ligands [8]. The study show the rational design of ligands around Ir center may change the hydrophobic and hydrophilic of complexes, and therefore change biological targets, and even the performance in cells [9]. And also, compared with simple cyclopentadiene (Cp), tetramethyl(biphenyl)cyclopentadienyl (Cp^{xbiph}), the diphenyl derivatives of Cp and showing the stronger electron donor characteristics, could further enhance the rate of ligand exchange and hydrolyze rapidly for complexes after introduction, therefore improving the overall antitumor activity [1,10]. In addition, the favorable targeted fluorescence characteristics of half-sandwich Ir^{III} complexes provided an insight into microscopic mechanism, after which enter the tumor cell organelles and target mitochondria, lysosomes and other tissues [8,11].

Due to the strong complexation ability of nitrogen atom of pyridine and the oxygen atoms of carboxylate to various transition metal ions, α-picolinic acid (α-PA) has attracted extensive attention as a potential chelating ligand [12–15]. The study show complex containing α-PA chelating ligand could effectively improve the catalytic property for hydrolysis, reduction and oxidation [16,17]. And also, these types of complexes showed good biological applications, such as carcinostatic, antitumor, antiviral and antibacterial activity [18]. Above all, as the type of OˆN chelating ligands, α-PA and its derivatives were used to construct the half-sandwich structure Ir^{III} antitumor complexes (Fig. 1 and Table 1). Compared with *cis*-platin (21.3 μM) widely used in clinic, the introduction of α-PA could effectively adjust the hydrophilicity and lipophilicity of target complexes, and leading to the potential antitumor activity (IC_{50} value of the best was 4.41 ± 0.43 μM) [9,19]. In

* Corresponding authors.
E-mail addresses: chemlxc@163.com (X. Liu), liuzheqd@163.com (Z. Liu).

https://doi.org/10.1016/j.jinorgbio.2018.12.012
Received 15 October 2018; Received in revised form 2 December 2018; Accepted 21 December 2018
Available online 24 December 2018

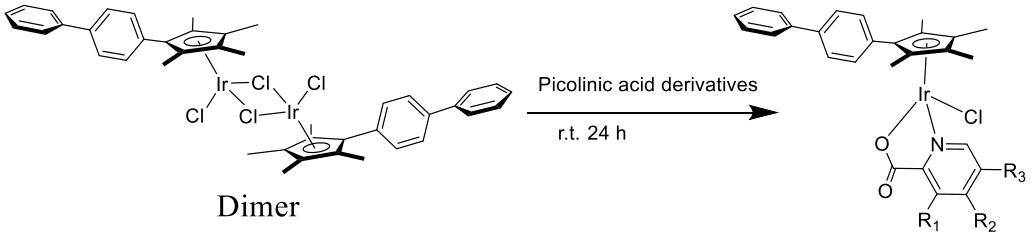

Fig. 1. Synthesis process of half-sandwich Ir^{III} α-PA complexes.

Table 1
IC_{50} values of Ir^{III} α-PA complexes, *cis*-platin and Dimer for 24 h.

Complexes	NˆO	IC_{50}(μM) A549 cells
[(η^5-Cp^{xbiph})Ir(L1)Cl] (**1**)	R_1 = H, R_2 = H, R_3 = H	31.3 ± 0.9
[(η^5-Cp^{xbiph})Ir(L2)Cl] (**2**)	R_1 = H, R_2 = H, R_3 = Br	5.6 ± 0.4
[(η^5-Cp^{xbiph})Ir(L3)Cl] (**3**)	R_1 = H, R_2 = Cl, R_3 = H	4. 9 ± 0.4
[(η^5-Cp^{xbiph})Ir(L4)Cl] (**4**)	R_1 = H, R_2 = H, R_3 = COOH	> 100
[(η^5-Cp^{xbiph})Ir(L5)Cl] (**5**)	R_1 = CH_3, R_2 = H, R_3 = H	15.7 ± 1.0
[(η^5-Cp^{xbiph})Ir(L6)Cl] (**6**)	R_1 = H, R_2 = H, R_3 = CF_3	4.4 ± 0.4
[(η^5-Cp^{xbiph})Ir(L7)Cl] (**7**)	R_1 = OH, R_2 = H, R_3 = H	15.4 ± 0.1
[(η^5-Cp^{xbiph})Ir(L8)Cl] (**8**)	R_1 = H, R_2 = H, R_3 = OH	43.8 ± 4.9
cis-Platin	/	21.3 ± 1.7
Dimer	/	57.7 ± 0.8

addition, complexes showed excellent bovine serum albumin (BSA) binding properties, and catalyzing the change of nicotinamide-adenine dinucleotid (NADH) to NAD^+. Due to the favorable targeted fluorescence, these complexes could also target mitochondria and lysosomes in A549 cells by the confocal microscopy imaging [20–22], and leading to the damage of lysosomes and the change of mitochondrial membrane potential. And also, energy-dependent cellular uptake mechanism is the main way for complexes to enter A549 tumor cells. The results suggest that α-PA-appended half-sandwich Ir^{III} complexes are hopeful for developing as new potential antitumor agents.

2. Results and discussion

Half-sandwich Ir^{III} α-PA complexes of the general formula [(η^5-Cp^{xbiph})Ir(NˆO)Cl] were synthesized at ambient temperature and obtained in good yields (61.0–79.0%) (Fig. 1 and Table 1). Target Ir^{III} complexes and the dimer of iridium were characterized by hydrogen nuclear magnetic resonance (^{1}H NMR) spectrum, mass spectrum (MS) and elemental analysis, and all the analytical data are consistent with the proposed structures (ESI Figs. S1–S2). Deuterated reagent DMSO (2.50 ppm) was used as a solvent for testing ^{1}H NMR of target complexes. The hydrogen on the five methyl groups on the Cp ring is shown in the range of 1.60 to 1.80 ppm in the ^{1}H NMR spectrum, while on the benzene ring and pyridine are shown in the range of 7.0 to 9.0 ppm. Other than that, target complexes used multiple solvents such as dichloromethane (5.76 ppm), methanol (3.16, 4.01 ppm), H_2O (3.33 ppm), ether (1.09, 3.38 ppm) or *n*-hexane (0.86, 1.25 ppm) in the synthesis and purification process, which showed a certain amount of residue in the ^{1}H NMR spectrum. Single crystal of complex **6** suitable for X-ray diffraction analysis was obtained by the slow diffusion of hexane into a saturated dichloromethane solution of complex. The X-ray crystal structures are shown in ESI Fig. S3, the crystallographic data and the selected bond lengths, bond angles are listed in ESI Tables S1 and S2, respectively. Complex **6** has the expected half-sandwich "three-leg piano-stool" geometry. The distances of iridium atom to η^5-cyclopentadienyl ring centroid were 1.747 Å. The Ir—Cl, Ir—O and Ir—N bond distances were 2.374(7), 2.153(19) and 2.050(2) Å, respectively. The larger bond length of Ir—Cl determines the weaker bond energy, which is convenient for the hydrolysis of half-sandwich Ir^{III} α-PA complex and provides the basis for better anticancer activity.

2.1. Cytotoxicity test

A549 cells were hatched in as-synthesized Ir^{III} complexes, and subsequently tested by the MTT (3-(4,5-dimethylthiazol-2-yl)-2,5-diphenyltetrazolium bromide) assay to evaluate the cytotoxicity. The IC_{50} values (the concentration of 50% cell growth is inhibited) are listed in Table 1 after hatched in Ir^{III} complexes and *cis*-platin for 24 h. Except for complex **4**, other complexes displayed higher potency against A549 lung tumor cells than the dimer. In addition, complex **6** showed the best activity (IC_{50}: 4.41 ± 0.43 μM), which was nearly 5 times of *cis*-platin (IC_{50}: 21.3 ± 1.7 μM) under the same conditions. The logP (partition coefficient in oil/water) values of complexes **1**, **4** and **6** were −0.15, −2.73 and 1.05, respectively, which were determined by inductively coupled plasma mass spectrometry (ICP-MS). Notably, compared with complex **1**, complex **4** improve lipophilicity by introducing hydrophilic carboxyl substituents to α-picolinic acid chelating ligand, which indicating that the stronger of hydrophobicity for complex **6** caused by trifluoromethyl (hydrophobic group), the greater of cytotoxicity.

2.2. Reaction with BSA

Serum albumin (SA), the most abundant protein in plasma, plays a crucial role in drug transport and metabolism [23,24]. The research on the interaction between Ir^{III} complexes and SA is conducive to study the antitumor mechanism of drugs. Bovine serum albumin (BSA) could be a cost-effective alternative model for human serum albumin (HSA) because of their similar structure, easy availability, and low price [24,25]. Therefore, in this study, complexes **1** and **6** were selected to study the binding ability with BSA by ultraviolet-visible (UV–Vis) absorption spectrum. As shown in Fig. 2a and ESI Fig. S4a, the maximum absorption at 218 nm decreased when increasing Ir^{III} complexes, which attributed to the interaction between Ir^{III} complex and BSA. Meanwhile, a significant red shift was found at 218 nm because of the influence of polar solvent (water) [26,27]. The increase in absorption at 278 nm is accompanied by the addition of complex, which indicate that the Ir^{III} α-PA complexes induces the changes of BSA in three aromatic acid residues (Tryptophan, tyrosine, and phenylalanine) [28–31].

Information on tyrosine or tryptophan residued in BSA could be determined by a synchronous fluorescence spectrophotometer at a wavelength interval of $\Delta\lambda$ = 15 nm and $\Delta\lambda$ = 60 nm, respectively. The weaked of fluorescence intensity at 291 nm and 285 nm ($\Delta\lambda$ = 15 nm and 60 nm, respectively) for complexes **1** and **6** were shown in ESI Figs. S5–S6. As shown, there is barely change at the wavelength of $\Delta\lambda$ = 60 nm, but a shift of 2–3 nm occurs at $\Delta\lambda$ = 15 nm, which indicate that tyrosine residued in BSA is more involved in the binding reaction than tryptophan.

The binding properties between Ir^{III} α-PA complexes and BSA could also be reflected by fluorescence emission spectroscopy. As shown in Fig. 2b (ESI Fig. S4b), with the increase of complexes **1** and **6** at 298 K, a rapid weaken of the fluorescence intensity for BSA was occurred. The Stern–Volmer quenching constant K_{sv}, quenching rate constant K_q, the binding constant K_b and binding site number n were calculated by classical Stern-Volmer equation (ESI Fig. S7) and Scatchard equation (ESI Fig. S8). Among these, the values of K_q were 2.87×10^{13} and

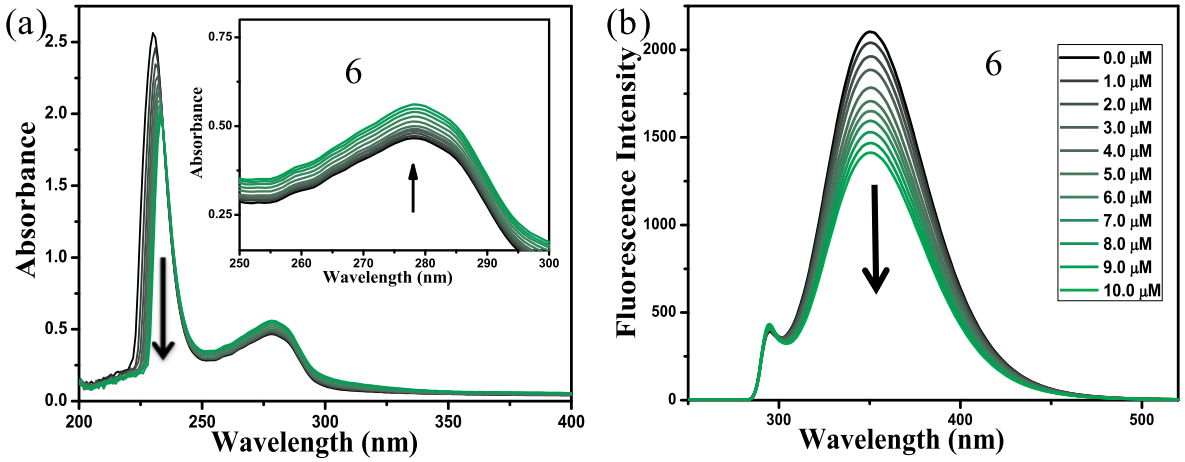

Fig. 2. (a) Absorbance of BSA (10 μM) was detected by UV–Vis spectrum after reaction with complex **6** (0–10 μM) in Tris-HCl/NaCl buffer solution (pH = 7.2) at 298 K. The arrows showed the change of absorbance with the increase of complex. Inset: Wavelength absorbance changes from 250 to 300 nm. (**b**) The fluorescence intensity of BSA (10 μM) was detected by fluorescence spectra after reaction with complex **6** (0–10 μM) in Tris-HCl/NaCl buffer solution (pH = 7.2) at 298 K. The arrows showed the change fluorescence intensity with the increase of complex.

Table 2
The values of K_{sv}, K_b, K_q and n for complexes **1** and **6** at 298 K.

Complexes	K_{sv} ($10^5\,M^{-1}$)	K_q ($10^{13}\,M^{-1}\,S^{-1}$)	K_b (M^{-1})	n
1	2.87 ± 0.18	2.87	4.23×10^4	0.85
6	4.95 ± 0.14	4.95	3.14×10^5	1.20

$4.95 \times 10^{13}\,M^{-1}\,s^{-1}$ for complexes **1** and **6**, respectively, which were almost three orders of magnitude higher than that of a pure dynamic quenching mechanism ($2.0 \times 10^{10}\,M^{-1}\,s^{-1}$) in Table 2 [32]. The results indicate that static quenching mechanism is the main way for Ir^{III} α-PA complexes acting on BSA. And also, complex **6** had a larger binding constant (K_b) value and binding site number (n) than complex **1**, which was consistent with that complex **6** showing the better antitumor activity.

2.3. Interaction with ctDNA

To understand whether the selected complexes **1** and **6** have a possible binding to DNA, the interaction of the complex with ctDNA (DNA sodium from the calf thymus) was investigated by UV–Vis titration, meanwhile, the binding constant (K_b) was calculated [33]. As shown in Table 3 and ESI Fig. S9, with the increase of ctDNA, the decrease of absorption value and small red shift (Δλ) at 262 nm were found, which concluded that the base pair interacted with Ir^{III} complex was informed by electrostatic-binding or non-covalent insertion [34]. The binding constants K_b were obtained by Benesi–Hildebrand equation [26]. As shown, compared with complex **1**, the introduction of trifluoromethyl substituent induces the greater K_b for complex **6**, which was consistent with the change of antitumor activity. Antitumor metallodrugs binding with DNA usually leads to hypochromism and bathchromism, due to the intercalative mode involving a strong stacking interaction between aromatic chromophore and the base pairs of DNA [35]. The extent of the hypochromism commonly parallels the intercalative binding strength [36]. As shown in Table 3, with the increase of DNA, the spectral perturbation follows the order: complex **1** > **6**. Although Ir^{III} α-PA complexes could interact with ctDNA probably via noncovalent binding modes, DNA could not be the main target due to the absence of formation of nucleobase adducts and plasmid DNA cleavage. These findings suggested that DNA-complex interaction was a possible cause of antitumor activity.

Table 3
Absorption spectroscopic properties of the Ir^{III} complexes with ctDNA.

Complexes	Absorption λ_{max} (nm)		Δλ	Hypochromicity (%)	K_b ($10^4\,mM^{-1}$)
	Free	Bound			
1	262	263	1	30.19	3.74
6	263	265	2	20.08	9.79

[Complex] = 20 μM at [DNA]/[Complex] = 20.

2.4. Reaction of complexes with NADH

The coenzyme, nicotinamide adenine dinucleotide (NADH), plays a vital role in the biocatalysis process [10]. Our previous study indicated that half-sandwich Ir^{III} complexes were able to catalyze the change of NADH to NAD^+ and induce the production of reactive oxygen species (ROS), which provide a pathway for the mechanism of oxidation [37,38]. The interaction between NADH and Ir^{III} α-PA complexes was obtained by UV–Vis spectrum in Fig. 3 (ESI Fig. S10). A slight decrease in 339 nm and increase in 259 nm (the absorbance of NADH and NAD^+, respectively [38]) were obtained with the increase of complexes. The turnover numbers (TONs) of complexes **1** and **6** were shown in Fig. 3b. Complex **6** show the bigger TON value (7.09) than **1** (5.95), which was correspond with the result of MTT assay.

2.5. Apoptosis assay

Flow cytometry was used to determine whether cell function decline was associated with apoptosis by means of A549 cells treated with Ir^{III} complexes after stained with annexin V-FITC and Propidium iodide [39,40]. As shown in Fig. 4 and ESI Tables S3–S4, the values of the early and late apoptotic phase had a significant increase when the concentration of complex **6** changed from 1.0 × IC_{50} to 3.0 × IC_{50} after 24 h (from 2.6% and 12.6% to 3.4% and 80.2%, respectively). In comparison, approximately 30.6% of A549 cells treated with complex **1** were undergoing apoptosis, of which 29.1% were in late apoptosis, however, 92.8% survived for control under the same conditions. The results were consistent with the results of MTT assay, and further confirmed Ir^{III} α-PA complexes could lead to function decline of tumor cells and induce apoptosis.

2.6. Cell cycle analysis

The cell cycle was monitored to determine whether cell cycle arrest

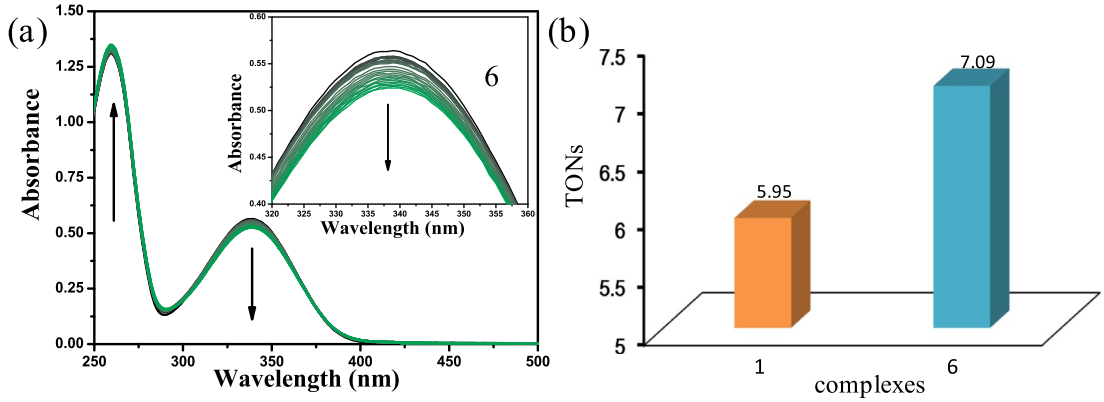

Fig. 3. (a) Absorbance of NADH (100 μM) was detected by UV–Vis spectrum after reaction with complex **6** (1 μM) in methanol solution (MeOH/H_2O = 20%/80% (V:V)) at 298 K for 8 h. Inset: Wavelength from 220 to 260 nm. The arrows showed absorbance changed over time. (b) The histogram of TONs for complexes **1** and **6**.

was caused by the antiproliferative activity of Ir^{III} complexes [41,42]. As shown in Fig. 5 (ESI Tables S5–S6), the results of cell cycle arrest for A549 cells were determined by flow cytometry after 24 h with different concentration (0.25, 0.5, 1.0 and 2.0 × IC_{50} for complexes **1** and **6**). As shown, the percentages of cells in G_0/G_1 + G_2/M phase increased by only 1.1% at the concentration of 2.0 × IC_{50} for complex **1**. However, for complex **6**, which increased by 16.9%. Compared with the control, Ir^{III} *α*-PA complexes can interfere with the cell growth cycle progression of G_0/G_1 + G_2/M phase, and achieving the purpose of apoptosis.

2.7. Induction of ROS

The ROS levels of A549 tumor cells hatched in complexes **1** and **6** (0.25 and 0.5 × IC_{50}) were detected by flow cytometry. As shown in Fig. 6 (ESI Tables S7–S8), compared with the control, there is hardly no change for the ROS level. These results were consistent with the conclusion of the NADH test, the oxidation is not the main mechanism for the antitumor activity of Ir^{III} *α*-PA complexes.

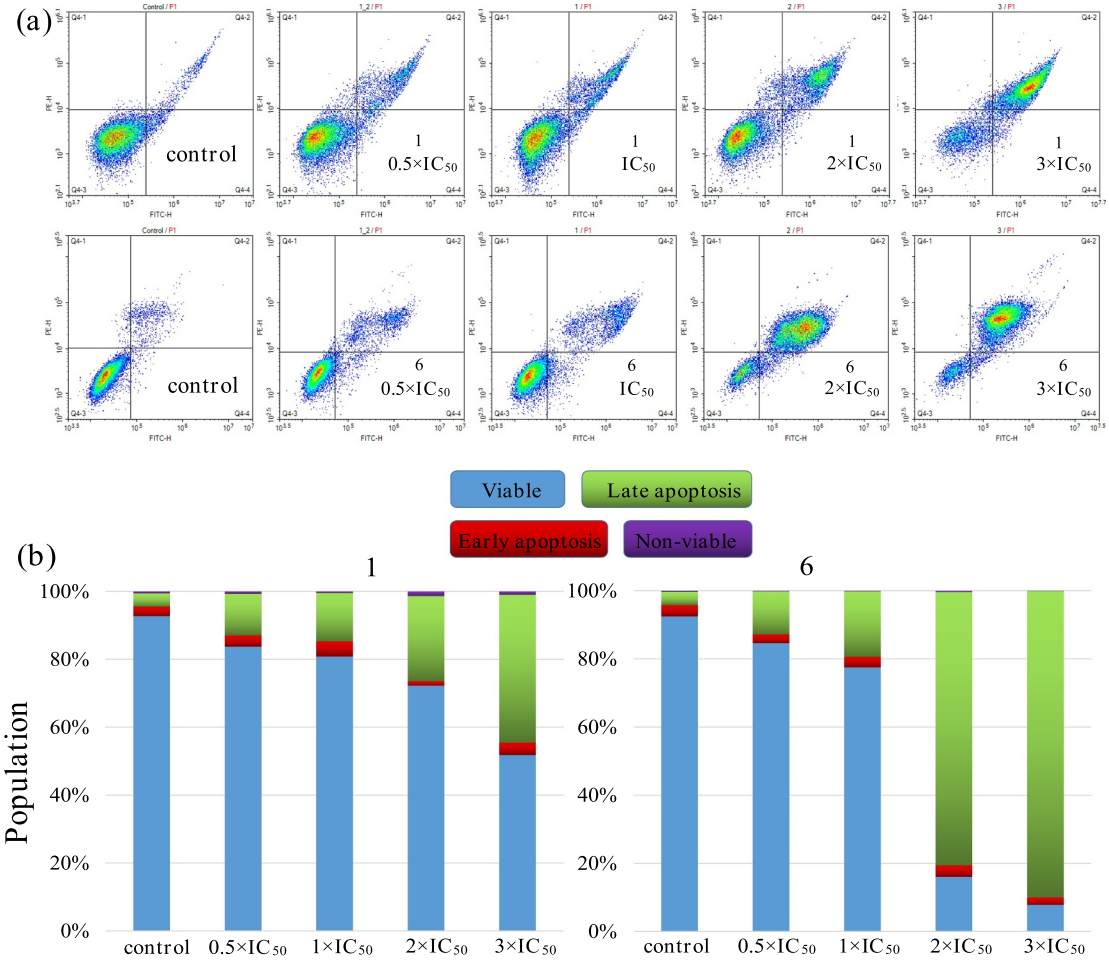

Fig. 4. (a) Apoptosis of A549 cells was analyzed by flow cytometry after treated with complexes **1** and **6** (concentrations = 0.5, 1.0, 2.0 × IC_{50}, 3.0 × IC_{50}) and annexin V-FITC and PI stained for 24 h at 310 K. (b) The histogram of four stages for A549 cells induced by complexes **1** and **6**. Data was averaged for three replicate experiments ± SD.

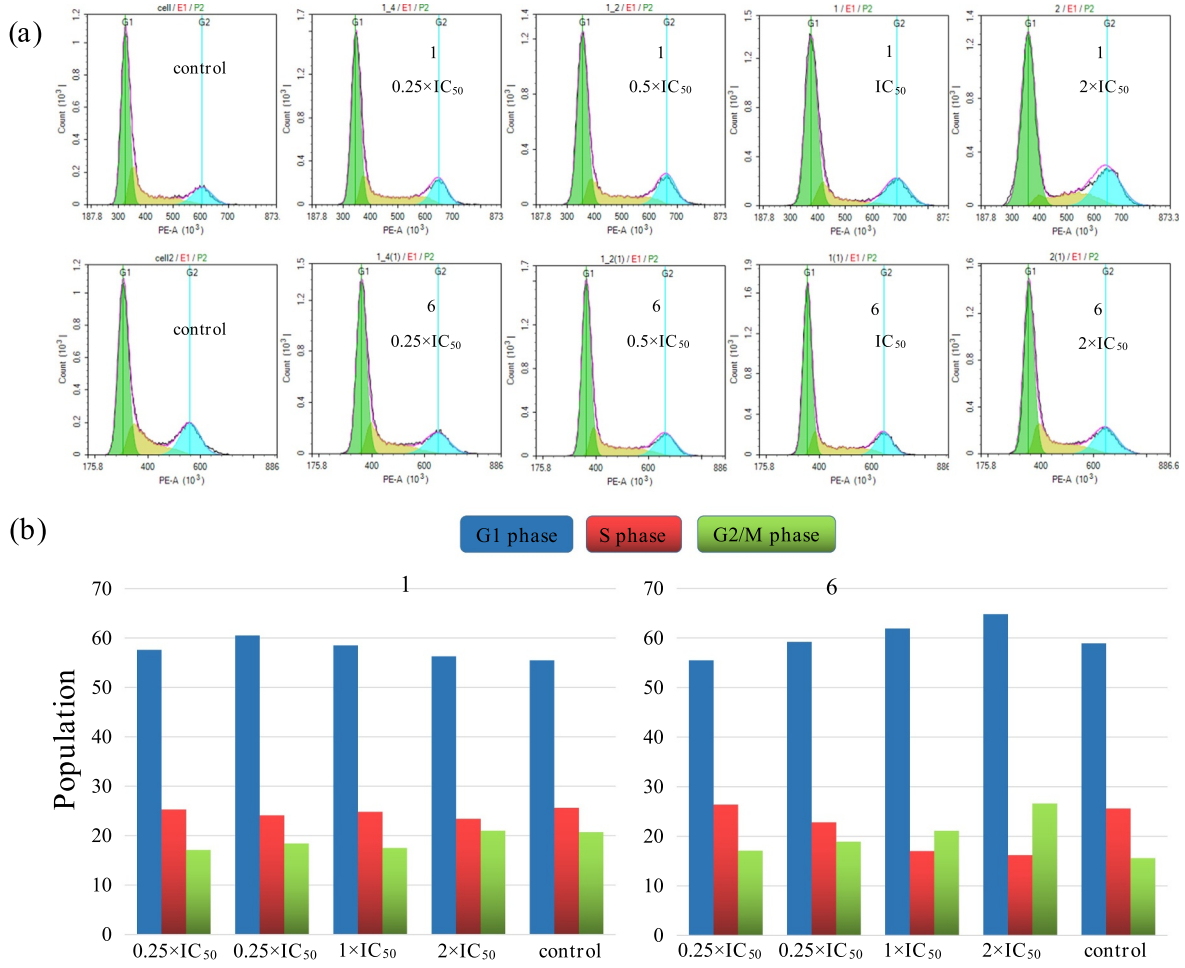

Fig. 5. (a) The altered A549 cell cycle was analyzed by flow cytometry after induced by complexes **1** and **6** (concentrations = 0.25, 0.5,1.0 and 2.0 × IC_{50}) for 24 h at 310 K. (b) The histogram of cell cycle distributions. Data are quoted as mean ± SD of three replicates.

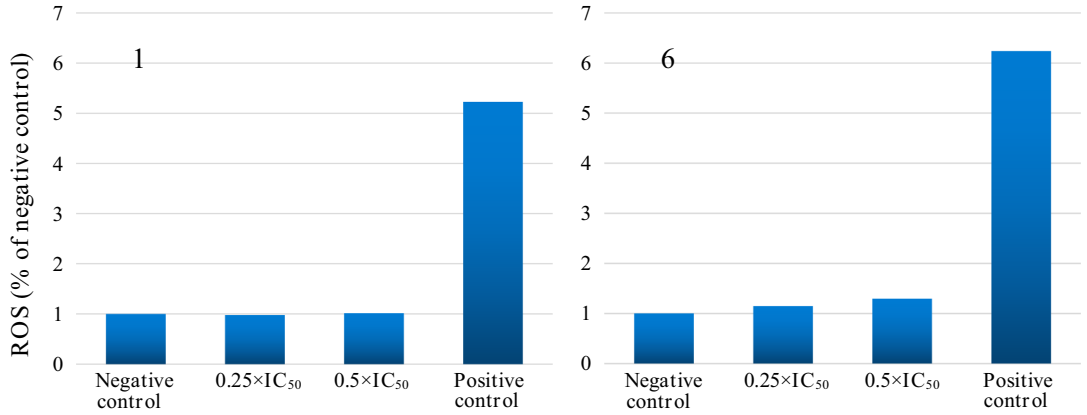

Fig. 6. The histogram of ROS level to A549 tumor cells hatched by complexes **1** and **6** (concentrations = 0.25, 0.5, 1.0 and 2.0 × IC_{50}). Data was averaged for three replicate experiments ± SD.

2.8. Mitochondrial membrane potential (ΔΨm)

Mitochondria provided energy for the life activities of cells and were the main sites for the formation of adenosine triphosphate (ATP) in cells [42]. Mitochondrial dysfunction could lead to cell death, and the change of mitochondrial membrane potential ($\Delta\Psi_m$) was usually used to assess [43]. The values of $\Delta\Psi_m$ were determined through evaluating the change of JC-1 (a frequently-used fluorescent probe to assess $\Delta\Psi_m$) when A549 cells were hatched in complexes **1** and **6** (the concentrations of 0.25, 0.5, 1.0 and 2.0 × IC_{50}) and subsequently stained. As shown in Fig. 7 and ESI Tables S9–S10, a significant concentration-dependent increase was found at the indicated concentrations, with a remarkable loss from 6.73% and 5.46% (control) to 29.71% and 82.08% (2.0 × IC_{50}) for complexes **1** and **6**, respectively. This conclusion is reflected more intuitively by the ratios of JC-1 Monomers (Green)/JC-1 Aggregates (Red) in Fig. 7b, which further confirmed Ir^{III} α-PA complexes could act on target mitochondria and induced apoptosis.

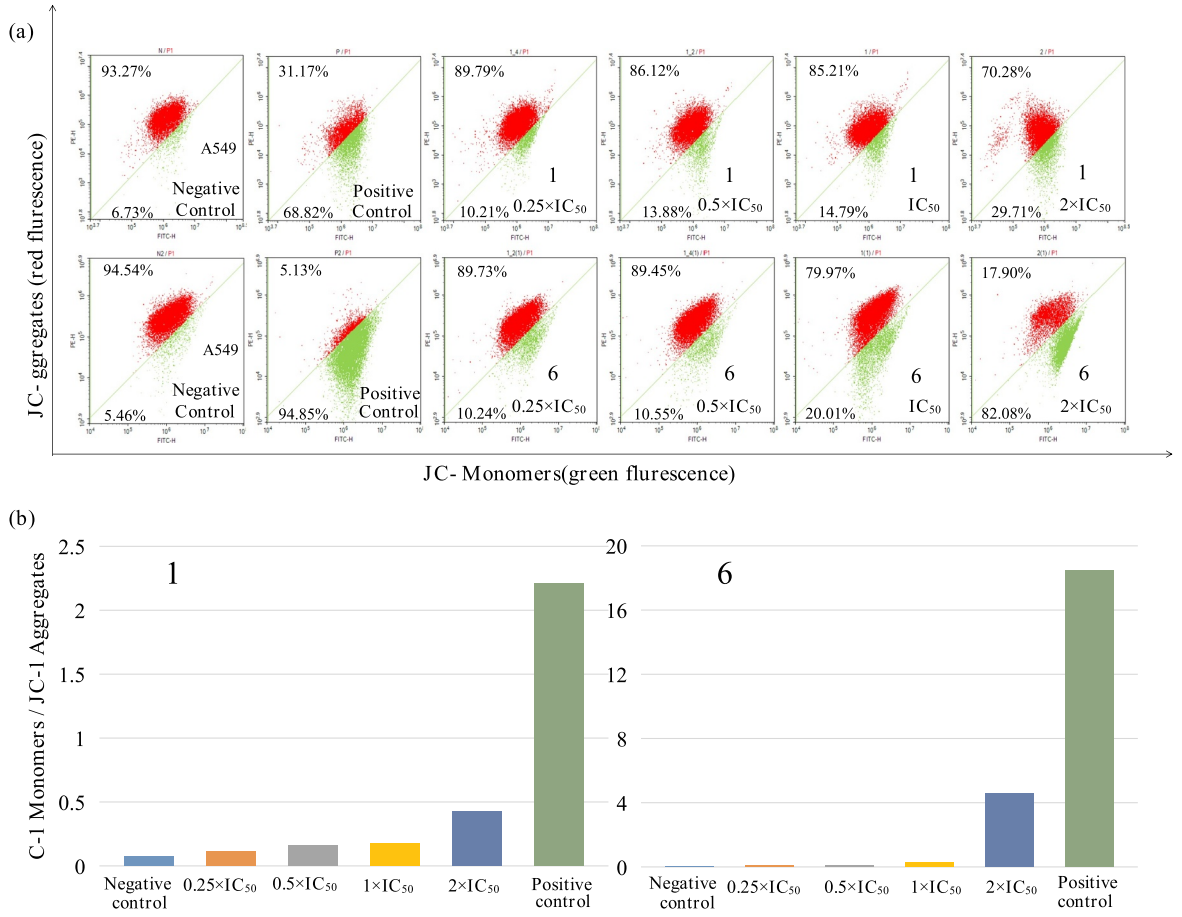

Fig. 7. (a) Changes in mitochondrial membrane potential of A549 tumor cells induced by complexes **1** and **6** (concentrations = 0.25, 0.5, 1.0 and 2.0 × IC_{50}). (b) Histograms for the JC-1 Monomers/JC-1 Aggregates (the ratios of green to red fluorescence) treated with complexes **1** and **6**. Data are quoted as mean ± SD of three replicates.

2.9. Cell imaging and cellular uptake mechanism

Laser confocal microscopy was used to determine the subcellular localization in A549 cells due to the inherent luminescence property for Ir^{III} α-PA complex [43]. The mitochondrial and lysosomal fluorescent probes were Mito Tracker Deep Red (MTDR) and Lyso Tracker Red DND-99 (LTRD) [45,45], respectively. As shown in Fig. 8a, complex **6** could effectively target lysosomes with a high Pearson's colocalization coefficient (PCC) of 0.74. On the other hand, complex **6** could also target mitochondria with the PCC value of 0.33. Interestingly, Ir^{III} α-PA

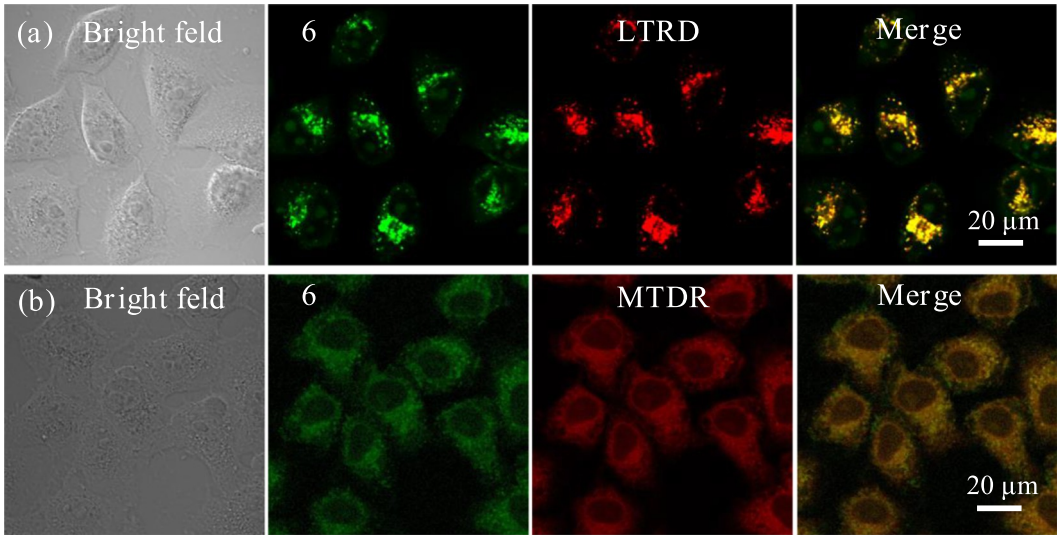

Fig. 8. (a) Confocal laser images of A549 cells hatched in complex **6** (15 μM, 1 h) and LTRD (100 nM, 30 min). (b) Confocal laser images of A549 cells hatched in complex **6** (15 μM, 1 h) and MTDR (50 nM, 30 min). Scale bars: 20 μm.

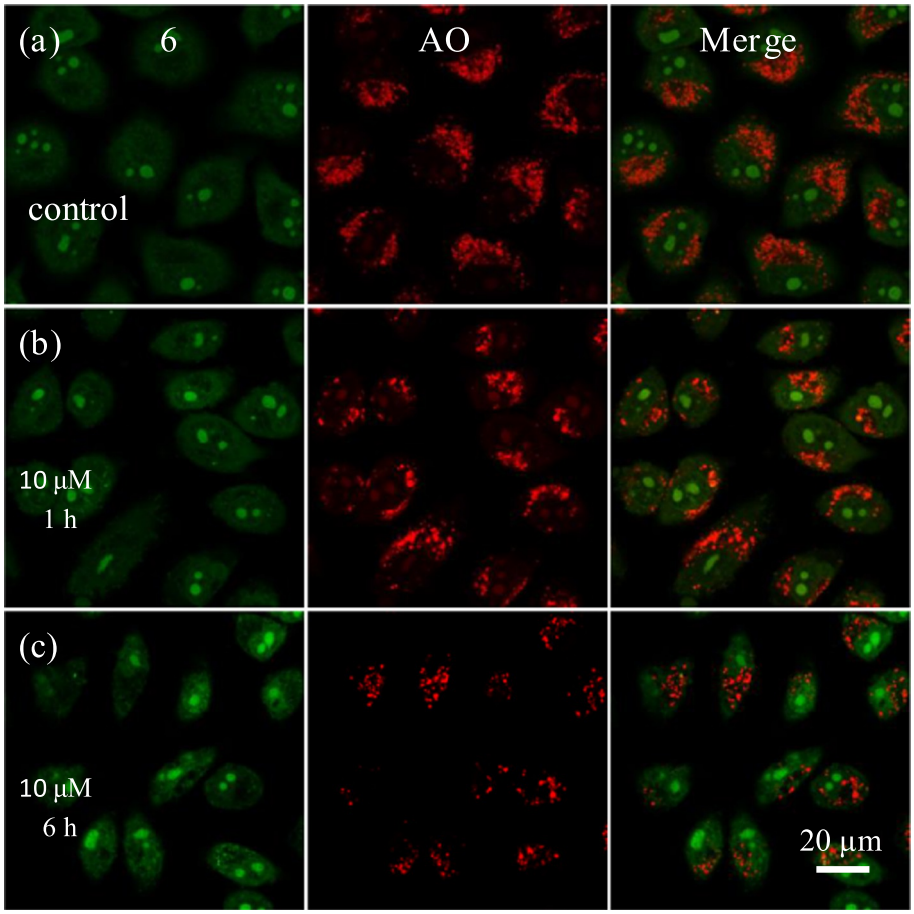

Fig. 9. Laser confocal microscopy images of A549 cells after hatched in complex **6** and stained by AO. (a) A549 cells were stained by AO (5 μM). (b) A549 cells were hatched in complex **6** (10 μM) for 1 h and then stained by AO (5 μM). (c) A549 cells were hatched in complex **6** (10 μM) for 6 h and then stained by AO (5 μM). λ_{ex} = 488 nm, λ_{em} = 510 ± 30 nm (green) and 625 ± 30 nm (red). Scale bar: 20 μm.

complex did not cause abnormal cell death immediately, which made it easy to track the changes in cells in real time.

Compared with normal cells, most of the lysosomal changes are caused by tumor suppressor genes in tumor cells [46]. Therefore, researchers have shown a high interest in studying the effects of lysosomal destruction on tumor cell death and tumor cell apoptosis mechanisms [47,48]. Drug-treated A549 cells were stained by acridine orange (AO, an effective probe to research lysosomal integrity due to its characteristics with red fluorescence in the lysosomes and green fluorescence in the cytoplasm and nucleus.) to test the lysosomal integrity. As shown in Fig. 9, there was a significant decrease for red fluorescence in lysosomes when A549 cells hatched in complex **6** (1.0 × IC_{50}) for 1 h, and obvious lysosomal damage was found after 6 h. The results confirmed that Ir^{III} *α*-PA complexes could target lysosomes, induce lysosomal damage, and eventually lead to apoptosis.

Energy demand mechanisms (divided into active transport and endocytosis) and non-energy demand mechanisms (divided into passive transport and free diffusion) were two major cellular uptake mechanisms for drugs [48]. Chloroquine and carbonyl cyanide *m*-chlorophenylhydrazine (CCCP) were selected as the endocytosis inhibitor and the energy inhibitor to study the uptake mechanism of complexes, respectively [49]. Cells should be incubated for 2 h at 277 K and 310 K before pre-treating cells with chloroquine and CCCP. The ingestion efficiency of A549 tumor cells was lowered at 277 K compared to the cells at a temperature of 310 K, from which it was seen that the complex **6** was taken up by cells to follow the energy demand mechanism as shown in Fig. 10.

3. Conclusions

In this paper, eight half-sandwich structure Ir^{III} *α*-PA complexes were synthesized and charactered by ^{1}H NMR, MS and element analysis. Target complexes showed the potential antitumor activity towards A549 tumor cells, and the best of which (complex **6**) was nearly five times *cis*-platin under the same conditions. Complexes could be transported by serum albumin, catalyze the conversion of NADH to NAD^+. Complexes could enter tumor cells by the means of energy-dependent mechanisms, specifically targeted lysosomes and mitochondria, eventually leaded to lysosomal damage and the change of mitochondrial membrane potential, disturbed the cell growth cycle and induced apoptosis. Above all, half-sandwich Ir^{III} *α*-PA complexes could be hopeful for a potential candidate for antitumor drugs.

4. Experimental section

4.1. Materials

$IrCl_3{\cdot}3H_2O$, butyllithium solution (1.6 M in hexane), 2,3,4,5-tetramethyl-2-cyclopentenone (95%), 4-bromobiphenyl, trimethyl(2,3,4,5-tetramethyl-2,4-cyclopentadien-1-yl)silane (97%) and different pyridine acid ligands (L1–L8) were purchased from Ruiya Technology Company Limited. DMEM medium, fetal bovine serum, penicillin/streptomycin mixture, trypsin/EDTA, and phosphate-buffered saline (PBS) were purchased from Sangon Biotech. Ir^{III} *α*-PA complexes was dissolved in DMSO and diluted with the tissue culture medium before use.

4.2. Synthesis of $[(\eta^5\text{-}C_5Me_4C_6H_4C_6H_5)IrCl_2]_2$ (dimer)

Dimer was prepared according to literature method [9]. A solution of Cp^{xbiph} (6.83 g, 25 mmol) and $IrCl_3{\cdot}nH_2O$ (7.33 g, 25 mmol) in MeOH (60 mL) was heated to reflux under N_2 atmosphere for 48 h. The dark

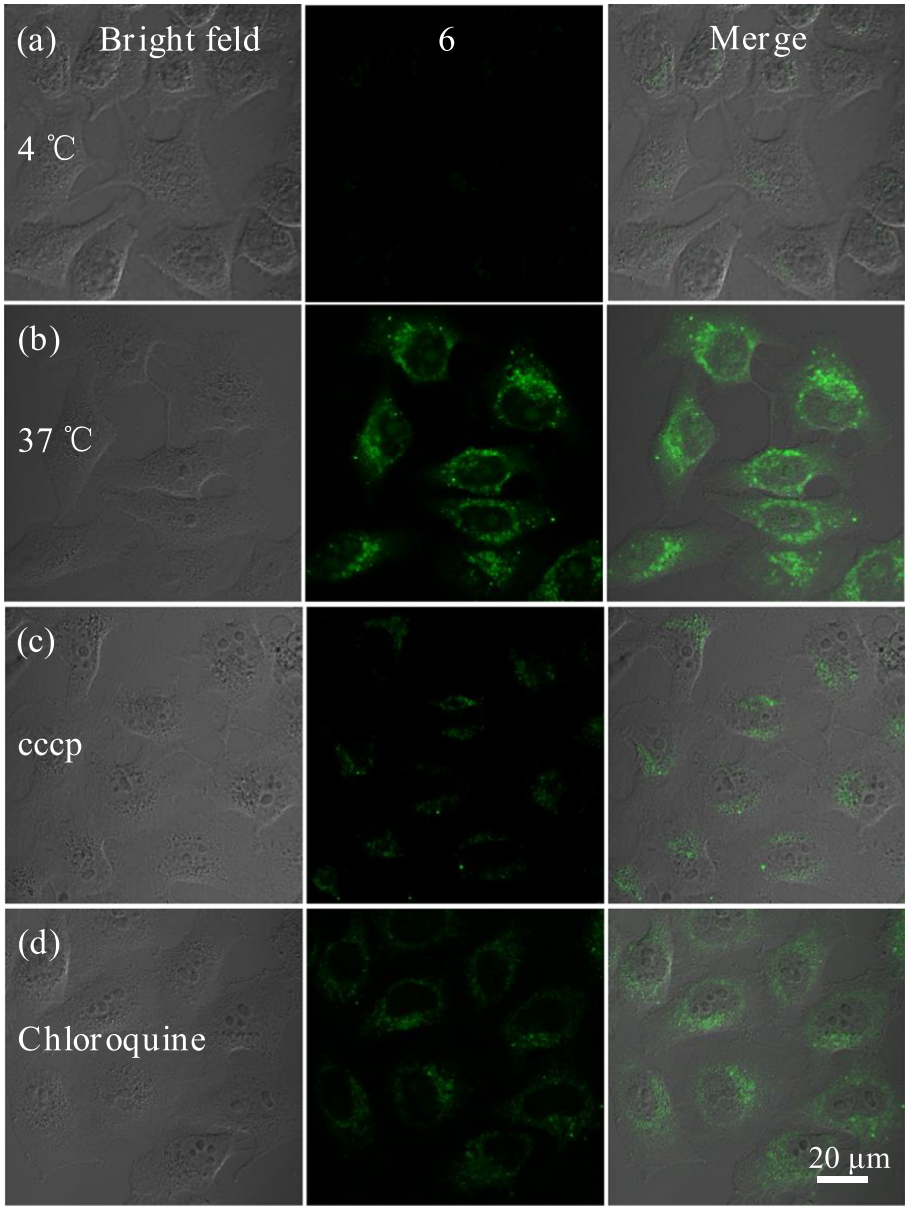

Fig. 10. Confocal images of A549 cells after hatched in complex **6** (10 μM) under different conditions. (a) A549 Cells were hatched in complex **6** (10 μM) for 10 min at 277 K. (b) A549 cells were hatched in complex **6** (10 μM) for 10 min at 310 K. (c) A549 cells were hatched in CCCP (10 μM) at 310 K for 1 h and then complex **6** (10 μM) at 310 K for 10 min. (d) A549 cells were hatched in chloroquine (50 μM) for 1 h at 310 K and then complex **6** (10 μM) for 10 min at 310 K (λ_{ex} = 405 nm, λ_{em} = 590 ± 30 nm). Scale bars: 20 μm.

red product was concentrated to 8 mL on a rotary evaporator. An orange crystal was precipitated at −5 °C. The product was collected by filtration, washed with dichloromethane and ether and dried in vacuo. Yield 52.2%. ^{1}H NMR (500 MHz, DMSO) δ 7.70 (qd, J = 8.6, 1.8 Hz, 6H), 7.48 (t, J = 7.7 Hz, 2H), 7.40 (d, J = 7.3 Hz, 1H), 1.72 (d, J = 14.5 Hz, 12H).

5. Synthesis of complexes 1–8

General procedure: Under N_2 atmosphere, [(η^5-$C_5Me_4C_6H_4C_6H_5$)$IrCl_2]_2$ (Dimer) (0.05 mmol) and α-PA chelating ligands (L1–L8) (0.10 mmol) are dissolved in methanol (40 mL) to obtain a mixed solution, which was stirred for 12 h at 37 °C (monitored by thin-layer chromatography). The solvent was removed on a rotary evaporator and recrystallized from methanol and ether. The crystalline pellets were washed with ether and dried. The ^{1}H NMR (500 MHz, DMSO) peak integrals of complexes **1–8** are shown in ESI Fig. S1. The MS of complexes **1–8** are shown in ESI Fig. S2.

[(η^5-Cp^{xbiph})Ir(L1)Cl] (**1**). Yield: 72.2%. ^{1}H NMR (500 MHz, DMSO) δ 8.69 (d, J = 5.2 Hz, 1H), 8.17 (td, J = 7.7, 1.3 Hz, 1H), 7.96 (d, J = 7.7 Hz, 1H), 7.78 (ddd, J = 7.4, 5.5, 1.5 Hz, 1H), 7.73 (d, J = 8.4 Hz, 4H), 7.63 (d, J = 8.3 Hz, 2H), 7.49 (t, J = 7.7 Hz, 2H), 7.40 (t, J = 7.4 Hz, 1H), 1.75 (d, J = 8.8 Hz, 6H), 1.68 (d, J = 17.7 Hz, 6H). ESI-MS (m/z): $[M\text{-}Cl]^+$ Calcd for $C_{27}H_{25}IrNO_2$, 587.72; Found 587.98. Elemental Analysis: found: C, 51.99; H, 4.01; N, 2.28%, calcd for $C_{27}H_{25}ClIrNO_2$: C, 52.04; H, 4.04; N, 2.25%.

[(η^5-Cp^{xbiph})Ir(L2)Cl] (**2**). Yield: 73.3%. ^{1}H NMR (500 MHz, DMSO) δ 8.64 (d, J = 1.9 Hz, 1H), 8.45 (dd, J = 8.3, 2.0 Hz, 1H), 7.90 (d, J = 8.3 Hz, 1H), 7.74 (t, J = 7.7 Hz, 4H), 7.62 (d, J = 8.3 Hz, 2H), 7.49 (t, J = 7.7 Hz, 2H), 7.40 (t, J = 7.4 Hz, 1H), 1.77 (d, J = 1.7 Hz, 6H), 1.69 (s, 6H). ESI-MS (m/z): $[M\text{-}Cl]^+$ Calcd for $C_{27}H_{24}BrIrNO_2$, 665.58; Found 665.96. Elemental Analysis: found: C, 46.12; H, 3.41; N, 2.07%, calcd for $C_{27}H_{24}BrClIrNO_2$: C, 46.19; H, 3.45; N, 2.00%.

[(η^5-Cp^{xbiph})Ir(L3)Cl] (**3**). Yield: 68.2%. ^{1}H NMR (500 MHz, DMSO)

δ 8.64 (d, J = 6.0 Hz, 1H), 8.00 (d, J = 2.4 Hz, 1H), 7.92 (dd, J = 6.0, 2.5 Hz, 1H), 7.76–7.71 (m, 4H), 7.64 (d, J = 8.3 Hz, 2H), 7.49 (t, J = 7.7 Hz, 2H), 7.40 (t, J = 7.4 Hz, 1H), 1.75 (d, J = 4.0 Hz, 6H), 1.68 (d, J = 17.7 Hz, 6H). ESI-MS (m/z): $[M\text{-}Cl]^+$ Calcd for $C_{27}H_{24}ClIrNO_2$, 622.16; Found 621.98. Elemental Analysis: found: C, 49.35; H, 3.64; N, 2.14%, calcd for $C_{27}H_{24}Cl_2IrNO_2$: C, 49.31; H, 3.68; N, 2.13%.

[(η^5-Cp^{xbiph})Ir(L4)Cl] (**4**). Yield: 61.0%. ^{1}H NMR (500 MHz, DMSO) δ 14.15 (s, 1H), 8.94 (d, J = 1.2 Hz, 1H), 8.57 (dd, J = 8.0, 1.6 Hz, 1H), 8.06 (d, J = 8.0 Hz, 1H), 7.74 (t, J = 7.4 Hz, 4H), 7.67 (d, J = 8.3 Hz, 2H), 7.49 (t, J = 7.6 Hz, 2H), 7.40 (t, J = 7.4 Hz, 1H), 1.75 (d, J = 1.2 Hz, 6H), 1.69 (d, J = 2.6 Hz, 6H). ESI-MS (m/z): $[M\text{-}Cl]^+$ Calcd for $C_{28}H_{25}IrNO_4$, 631.73; Found 631.96. Elemental Analysis: found: C, 50.38; H, 3.78; N, 2.12%, calcd for $C_{28}H_{25}ClIrNO_4$: C, 50.41; H, 3.78; N, 2.10%.

[(η^5-Cp^{xbiph})Ir(L5)Cl] (**5**). Yield: 78.8%. ^{1}H NMR (500 MHz, DMSO) δ 8.55 (s, 1H), 7.96 (s, 1H), 7.72 (s, 4H), 7.65 (s, 3H), 7.49 (s, 2H), 7.40 (s, 1H), 2.63 (s, 3H), 1.73 (d, J = 7.8 Hz, 6H), 1.66 (d, J = 18.6 Hz, 6H). ESI-MS (m/z): $[M\text{-}Cl]^+$ Calcd for $C_{28}H_{27}IrNO_2$, 601.75; Found 602.03. Elemental Analysis: found: C, 52.76; H, 4.24; N, 2.25%, calcd for $C_{28}H_{27}ClIrNO_2$: C, 52.78; H, 4.27; N, 2.20%.

[(η^5-Cp^{xbiph})Ir(L6)Cl] (**6**). Yield: 72.5%. ^{1}H NMR (500 MHz, DMSO) δ 8.70 (s, 1H), 8.65 (dd, J = 8.2, 1.5 Hz, 1H), 8.18 (d, J = 8.1 Hz, 1H), 7.77–7.71 (m, 4H), 7.65 (d, J = 8.3 Hz, 2H), 7.50 (t, J = 7.6 Hz, 2H), 7.41 (t, J = 7.3 Hz, 1H), 1.78 (s, 6H), 1.71 (d, J = 14.4 Hz, 6H). ESI-MS (m/z): $[M\text{-}Cl]^+$ Calcd for $C_{28}H_{24}F_3IrNO_2$, 655.72; Found 656.02. Elemental Analysis: found: C, 48.72; H, 3.48; N, 2.01%, calcd for $C_{28}H_{24}ClF_3IrNO_2$: C, 48.66; H, 3.50; N, 2.03%.

[(η^5-Cp^{xbiph})Ir(L7)Cl] (**7**). Yield: 77.3%. ^{1}H NMR (500 MHz, DMSO) δ 12.83 (s, 1H), 8.22 (dd, J = 3.6, 2.7 Hz, 1H), 7.75 (dd, J = 8.4, 6.7 Hz, 4H), 7.69–7.63 (m, 4H), 7.49 (t, J = 7.6 Hz, 2H), 7.40 (t, J = 6.8 Hz, 1H), 1.74 (d, J = 2.1 Hz, 6H), 1.68 (d, J = 15.6 Hz, 6H). ESI-MS (m/z): $[M\text{-}Cl]^+$ Calcd for $C_{27}H_{25}IrNO_3$, 603.72; Found 603.99. Elemental Analysis: found: C, 50.72; H, 3.91; N, 2.23%, calcd for $C_{27}H_{25}ClIrNO_3$: C, 50.74; H, 3.94; N, 2.19%.

[(η^5-Cp^{xbiph})Ir(L8)Cl] (**8**). Yield: 66.4%. ^{1}H NMR (500 MHz, DMSO) δ 11.30 (s, 1H), 8.14 (d, J = 2.5 Hz, 1H), 7.77 (d, J = 8.6 Hz, 1H), 7.74 (d, J = 8.4 Hz, 4H), 7.64 (d, J = 8.3 Hz, 2H), 7.48 (dd, J = 12.7, 4.8 Hz, 3H), 7.40 (t, J = 7.4 Hz, 1H), 1.73 (s, 6H), 1.66 (d, J = 15.3 Hz, 6H). ESI-MS (m/z): $[M\text{-}Cl]^+$ Calcd for $C_{28}H_{29}IrNO_3$, 603.72; Found 604.00. Elemental Analysis: found: C, 50.71; H, 3.94; N, 2.20%, calcd for $C_{27}H_{25}ClIrNO_3$: C, 50.74; H, 3.94; N, 2.19%.

Abbreviations

Ir^{III}	iridium^{III}
α-PA	α-picolinic acid
HSA	human serum albumin
BSA	bovine serum albumin
K_{sv}	Stern–Volmer quenching constant
K_q	quenching rate constant
K_b	binding constant
NADH	nicotinamide adenine dinucleotide
ICP-MS	inductively coupled plasma mass spectrometry
logP	partition coefficient in oil/water
UV–Vis	ultraviolet-visible spectrum
TONs	turn over numbers
MTT	3-(4,5-Dimethylthiazol-2-yl)-2,5-diphenyltetrazolium bromide
ROS	reactive oxygen species
$\Delta\Psi m$	mitochondrial membrane potential
PCC	Pearson's colocalization coefficient
MTDR	Mito Tracker Deep Red
LTRD	Lyso Tracker Red DND - 99
CCCP	m-chlorophenylhydrazone
AO	acridine orange

Acknowledgments

We thank the National Natural Science Foundation of China (Grant No. 21671118), the Taishan Scholars Program, the University Research Development Program of Shandong Province (J18KA082), and the Student's Platform for Innovation and Entrepreneurship Training Program of Shandong Province (201710446042) for support.

Notes

The authors declare no competing financial interest.

Appendix A. Supplementary data

Supplementary data to this article can be found online at https://doi.org/10.1016/j.jinorgbio.2018.12.012.

References

[1] S. Mukhopadhyay, R.K. Gupta, R.P. Paitandi, N.K. Rana, G. Sharma, B. Koch, L.K. Rana, M.S. Hundal, D.S. Pandey, Organometallics 34 (2015) 100–107.
[2] R.R. Barefoot, J. Chromatogr. B Biomed. Sci. Appl. 751 (2001) 205–211.
[3] E. Wong, C.M. Giandomenico, Chem. Rev. 99 (1999) 2451–2466.
[4] M. Callari, J.R. Aldrich-Wright, P.L.D. Souza, M.H. Stenzel, Prog. Polym. Sci. 39 (2014) 1614–1643.
[5] X.C. Liu, Y.H. Tang, X.D. He, X.X. Ge, J. Liu, X.Y. Meng, M.X. Shao, Y.M. Jin, L.J. Tian, Z. Liu, J. Inorg. Biochem. 191 (2019) 194–202.
[6] V. Novohradsky, L. Zerzankova, J. Stepankova, A. Kisova, H. Kostrhunova, Z. Liu, P.J. Sadler, J. Kasparkova, V. Brabec, Metallomics 6 (2014) 1491–1501.
[7] X. He, M. Tian, X. Liu, Y. Tang, C. Shao, P. Gong, J. Liu, S. Zhang, L. Guo, Z. Liu, Chem. Asian J. 13 (2018) 1500–1509.
[8] X. He, X. Liu, Y. Tang, J. Du, M. Tian, Z. Xu, X. Liu, Z. Liu, Dyes Pigments 160 (2019) 217–226.
[9] Z. Liu, A. Habtemariam, A.M. Pizarro, S.A. Fletcher, A. Kisova, O. Vrana, L. Salassa, P.C. Bruijnincx, G.J. Clarkson, V. Brabec, J. Med. Chem. 54 (2011) 3011–3026.
[10] Z. Liu, I. Romerocanelón, B. Qamar, J.M. Hearn, A. Habtemariam, N.P. Barry, A.M. Pizarro, G.J. Clarkson, Angew. Chem. Int. Ed. 53 (2014) 3941–3946.
[11] Z. Xu, D. Kong, X. He, L. Guo, X. Ge, X. Liu, H. Zhang, J. Li, Y. Yang, Z. Liu, Inorg. Chem. Front. 5 (2018) 2100–2105.
[12] H. Imam, B. Kumar, Shafayat, Orient. J. Chem. 27 (2011) 287–291.
[13] S.M. Shohayeb, R.G. Mohamed, H. Moustafa, S.M. El-Medani, J. Mol. Struct. 1119 (2016) 442–450.
[14] M.A. Yurovskaya, O.D. Mit'Kin, F.V. Zaitseva, Review, Chem. Heterocycl. Compd. 34 (1998) 871–899.
[15] A. Salvini, P. Frediani, E. Rivalta, Inorg. Chim. Acta 351 (2003) 225–234.
[16] R.I. Kureshy, N.H. Khan, S.H.R. Abdi, S.T. Patel, P. Iyer, J. Mol. Catal. A Chem. 150 (1999) 163–173.
[17] R. Ramesh, Inorg. Chem. Commun. 7 (2004) 274–276.
[18] P. Viswanathamurthi, K. Natarajan, Transit. Met. Chem. 24 (1999) 638–641.
[19] D. Xu, Y. Xu, N. Cheng, X. Zhou, Y. Shi, Q. He, J. Coord. Chem. 63 (2010) 2360–2369.
[20] Y. Li, B. Liu, X.R. Lu, M.F. Li, L.N. Ji, Z.W. Mao, Dalton Trans. 46 (2017) 11363–11371.
[21] R.R. Ye, C.P. Tan, M.H. Chen, L. Hao, L.N. Ji, Z.W. Mao, Chem. Eur. J. 22 (2016) 7800–7809.
[22] J. Adler, I. Parmryd, Cytometry A 77 (2010) 733–742.
[23] V. Thamilarasan, P. Karunakaran, N. Kavitha, C. Selvaraju, N. Sengottuvelan, Polyhedron 118 (2016) 12–24.
[24] B.P. Espósito, R. Najjar, Coord. Chem. Rev. 232 (2002) 137–149.
[25] T. Keleş, B. Barut, Z. Biyiklioglu, A. Özel, Dyes Pigments 139 (2017) 575–586.
[26] J. Li, L. Guo, Z. Tian, M. Tian, S. Zhang, K. Xu, Y. Qian, Z. Liu, Dalton Trans. 46 (2017) 15520–15534.
[27] R. Esteghamat-Panah, H. Hadadzadeh, H. Farrokhpour, J. Simpson, A. Abdolmaleki, F. Abyar, Eur. J. Med. Chem. 127 (2016) 958–971.
[28] D. Li, M. Zhu, C. Xu, B. Ji, Eur. J. Med. Chem. 46 (2011) 588–599.
[29] S. Tabassum, R. Singh, M. Zaki, M. Ahmad, M. Afzal, RSC Adv. 5 (2015) 35843–35851.
[30] X.F. Zhao, Y. Ouyang, Y.Z. Liu, Q.J. Su, H. Tian, C.Z. Xie, J.Y. Xu, New J. Chem. 38 (2014) 955–965.
[31] T.S. Kamatchi, P. Kalaivani, P. Poornima, V.V. Padma, F.R. Fronczek, K. Natarajan, RSC Adv. 4 (2013) 2004–2022.
[32] N.K. Das, L. Pawar, N. Kumar, S. Mukherjee, Chem. Phys. Lett. 635 (2015) 50–55.
[33] T. Mukherjee, M. Mukherjee, B. Sen, S. Banerjee, G. Hundal, P. Chattopadhyay, J. Coord. Chem. 67 (2014) 2643–2660.
[34] S.A.M. Sukri, L.Y. Heng, N.H.A. Karim, J. Fluoresc. 27 (2017) 1009–1023.
[35] P.K. CUmadevi, H. alaivani, S. Puschmann, P.S. Murugan, R. Mohan, J. Prabhakaran, Photochem. Photobiol. B 167 (2017) 45–57.
[36] Q.L. Zhang, J.G. Liu, H. Chao, G.Q. Xue, L.N. Ji, J. Inorg. Biochem. 83 (2001) 49–55.
[37] Z. Liu, R.J. Deeth, J.S. Butler, A. Habtemariam, M.E. Newton, P.J. Sadler, Angew.

Chem. Int. Ed. 125 (2013) 4288–4291.
[38] B.L. Soledad, L. Zhe, H. Abraha, A.M. Pizarro, Q. Bushra, P.J. Sadler, Angew. Chem. Int. Ed. 124 (2012) 3963–3966.
[39] W. Ma, X. Ge, L. Guo, S. Zhang, J. Li, X. He, Z. Liu, Dyes Pigments 162 (2019) 385–393.
[40] J. Li, Z. Tian, Z. Xu, S. Zhang, Y. Feng, L. Zhang, Z. Liu, Dalton Trans. 47 (2018) 15772–15782.
[41] M. Tian, J. Li, S. Zhang, L. Guo, X. He, D. Kong, H. Zhang, Z. Liu, Chem. Commun. 53 (2017) 12810–12813.
[42] A. Karabatsiakis, C. Böck, J. Salinas-Manrique, S. Kolassa, E. Calzia, D.E. Dietrich, I.T. Kolassa, Transl. Psychiatry 4 (2014) 397.
[43] Z. Tian, J. Li, S. Zhang, Y. Yang, Z. Xu, D. Kong, H. Zhang, X. Ge, J. Zhang, Z. Liu, Inorg. Chem. 57 (2018) 10498–10502.
[44] J. Li, L. Guo, Z. Tian, S. Zhang, Z. Xu, Y. Han, R. Li, Y. Li, Z. Liu, Inorg. Chem. 57 (2018) 13552–13563.
[45] Y. Han, Z. Tian, S. Zhang, X. Liu, J. Li, Y. Li, Y. Liu, M. Gao, Z. Liu, J. Inorg. Biochem. 189 (2018) 163–171.
[46] J. Wang, Y. Yu, K. Lu, M. Yang, Y. Li, X. Zhou, Z. Sun, Int. J. Nanomedicine 12 (2017) 809–825.
[47] Y. Zheng, L. He, D. Zhang, C. Tan, L. Ji, Z. Mao, Dalton Trans. 46 (2017) 11395–11407.
[48] C. Jin, J. Liu, Y. Chen, R. Guan, O. Cheng, Y. Zhu, L. Ji, H. Chao, Sci. Rep. 6 (2016) 22039.
[49] Y. Han, X. Liu, Z. Tian, X. Ge, J. Li, M. Gao, Y. Li, Y. Liu, Z. Liu, Chem. Asian J 13 (2018) 3697–3705.